



<http://www.diva-portal.org>

This is the published version of a paper published in *CIRP annals*.

Citation for the original published paper (version of record):

Dadbakhsh, S., Zhao, X., Chinnappan, P K., Shanmugam, V., Zeyu, L. et al. (2022)  
Process and geometrical integrity optimization of electron beam melting for copper  
*CIRP annals*, 71: 201-204  
<https://doi.org/10.1016/j.cirp.2022.03.041>

Access to the published version may require subscription.

N.B. When citing this work, cite the original published paper.

Permanent link to this version:

<http://urn.kb.se/resolve?urn=urn:nbn:se:kth:diva-312467>



# Process and geometrical integrity optimization of electron beam melting for copper

Sasan Dadbakhsh<sup>a,\*</sup>, Xiaoyu Zhao<sup>a</sup>, Prithiv Kumar Chinnappan<sup>a</sup>, Vishal Shanmugam<sup>a</sup>, Zeyu Lin<sup>a</sup>, Christopher Hulme<sup>b</sup>

<sup>a</sup> Production Engineering Department, KTH Royal Institute of Technology, Brinellvägen 68, Stockholm 11428, Sweden

<sup>b</sup> Department of Materials Science and Engineering, KTH Royal Institute of Technology, Brinellvägen 23, Stockholm 10044, Sweden

Submitted by B. Lindstrom (1), Sweden

## ARTICLE INFO

### Article history:

Available online 28 April 2022

### Keywords:

Additive Manufacturing  
Optimization  
Electron Beam Melting (EBM)

## ABSTRACT

This work systematically analyzes and optimizes the process of electron beam melting for pure copper. It is shown that, for reliable manufacturing, the preheating temperature should be optimized to avoid porosity as well as part deformation. The electron beam should be fully focused to prevent shrinkage voids (correlated to negative defocusing) and material spattering (linked to positive defocusing). Smoother surfaces from lower hatch spacing (e.g., 100 μm) can improve the density reliability, while longer overhangs are reached by a higher hatch spacing. A suitable starting contour strategy is also applied to mitigate border porosities, reduce side roughness and increase geometric precision.

© 2022 The Author(s). Published by Elsevier Ltd on behalf of CIRP. This is an open access article under the CC BY license (<http://creativecommons.org/licenses/by/4.0/>)

## 1. Introduction

Since additive manufacturing (AM) can produce complex components without any extensive machining or forming, it is used to make complex and highly conductive copper (Cu) components. The main laser-based AM technique to fabricate such components from powder is selective laser melting (SLM) [1–3]. However, Cu reflects the majority of the incident light from commercial fiber lasers. This limits the commercial production of highly conductive Cu parts [4]. One main design restriction in SLM is the need for the support structure to hold the down-facing surfaces (those commonly below 45°) such as overhangs and bridges [5].

Another popular AM method to manufacture bulk and porous metal components is electron beam melting (EBM). Similar to SLM, EBM is also a powder bed AM process, although it uses a very high-energy electron beam (EB) in a vacuum atmosphere to produce dense and complex parts. The commercial material palette of EBM is limited to titanium, CoCr and superalloys [6]. The limited material palette in EBM is due to the difficulties in optimizing the process parameters. The greatest difficulty is the sudden jumping of powder particles from the bed, known as smoking [7]. To prevent this, the powder bed is preheated to sinter the powder particles before melting. Since the sintering can be rather extensive, the as-built EBM surfaces are well-known to be rough and porous [8]. EBM also suffers from porosity, powder spattering, powder cake formation due to excessive sintering, loss of beam quality, geometric inaccuracy, metallization, process unreliability, varying part properties, thermal distortion and delamination.

More specifically for the case of Cu, EBM is less applied. This is despite the fact that EBM is much more energy efficient than commercial lasers, due to the latter's low efficiency and high back reflectivity. Nevertheless, some studies report that they have succeeded in manufacturing Cu components via EBM with almost 100%

density [9–11]. The high tendency of pure Cu to sinter can lead to powder sticking to the melt surfaces during powder dispersion [10]. Therefore, the process temperatures should be relatively low, which can influence and limit the ranges of other process parameters, including beam power and scan speed.

The same studies, however, fail to elaborate the challenges in EBM of Cu with its extremely high thermal conductivity (386 W m<sup>-1</sup> K<sup>-1</sup> as bulk, being several times higher than other metals), which may induce unreliability for industrial productions. Moreover, there is no report regarding the precision, accuracy and the geometrical possibilities of Cu parts produced by EBM. Accordingly, this work is dedicated to identify the processing challenges in respect to unrealized process parameters (such as beam focal point) affecting the reliability of Cu EBM parts. After comprehensive optimizations, the obtainable properties are recognized and the producible geometries are identified. Lastly, novel contouring strategies to improve the geometric precision and possibilities are examined. The ultimate goal is to realize an optimal technology in order to guaranty a smooth production with reliable properties and maximum geometrical flexibility.

## 2. Materials and methods

Gas atomized Cu powder (by Eckart GMBH) with 99.95% purity and particles with diameters 45–100 μm was used. The mean particle size was 61 μm in the virgin state and 52 μm after the powder was dispensed and recovered seven times (Fig. 1a,b). A Hall flowmeter was used to measure the flow time of 50 g powder at room temperature. The results showed a slight and gradual increase in the powder flow after the powder reuse (Fig. 1c).

EBM experiments were performed on this powder using an Arcam A2X machine. The filament voltage was 60 kV. An in-house developed 10 cm × 10 cm platform was retrofitted to the printer to reduce the powder use. The powder layer thickness was set at 50 μm. A rotation angle of 90° was applied between layers. Preliminary trials produced 10 mm cubic samples, with powder preheating at 310 °C, 400 °C, and 500 °C. The lower temperature

\* Corresponding author.

E-mail address: [sdad@kth.se](mailto:sdad@kth.se) (S. Dadbakhsh).

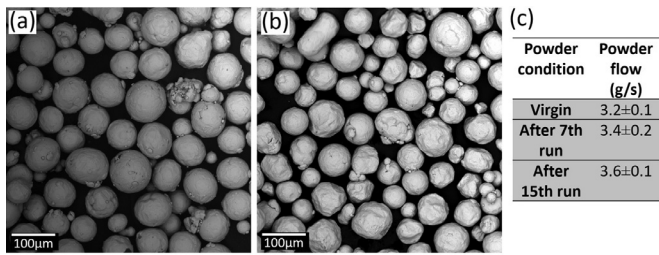


Fig. 1. (a) Virgin and (b) used (7th run) powder, and (c) the powder flow.

of 310 °C resulted in obvious porous parts (Fig. 2a) and occasional powder smoking, while 500 °C led to extra powder caking and geometrical deformation due to high lateral heat conduction (Fig. 2c). Therefore, further optimization was only carried out at 400 °C, which delivered high density in conjunction with good geometrical integrity and good build surfaces (Fig. 2b). Further optimization was performed by altering hatch spacing,  $h$ , focus offset, FO, scanning speed,  $s$ , and beam current,  $I$ . Beam power,  $P$  was derived as  $P = IV$ , where the voltage ( $V$ ) is 60 kV. Afterwards, the linear and surface input energy density,  $E$ , were estimated as  $E = P/s$  and  $E = P/(sh)$ .

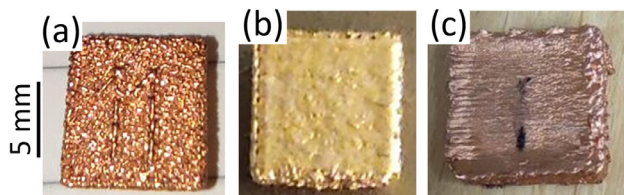


Fig. 2. Typical Cu EBM parts made with  $1.2 \text{ J mm}^{-1}$  linear energy density at preheating temperature of (a) 310 °C, (b) 400 °C, and (c) 500 °C.

Since density was the first parameter for process optimization, the Archimedes' principle was used to measure the density of the cubic parts using 99.5% pure isopropanol. After polishing, the cross sections were investigated using optical microscopy and scanning electron microscopy (SEM, Phenom ProX Desktop). Image analysis software (Image J) was applied to calculate the fraction of the porosity from cross sections. The microstructure was also viewed after etching using a solution consisting of 5 g ferric chloride, 10 ml 37% hydrochloric acid, 50 ml glycerol and 30 ml water at room temperature.

The surface roughness of the EBM Cu parts was measured using a white light interferometer (Zygo NewView™ 7300). The data were processed using Mountains®9 software (Digital Surf). Benchmark components (Fig. 3) were designed to analyze the geometrical integrity of the components, by identifying the capability of the process to manufacture thin walls, overhangs, thin rods, hollow features, etc. After manufacturing the benchmark parts, their geometrical properties were measured using 3D scanning by an ATOS Core 200 3D scanner with a resolution of 80 µm, controlled by the GOM software suite (Zeiss). After scanning, the results were compared with the original model using a separate surface synthesis software, Inspect, from the GOM suite.

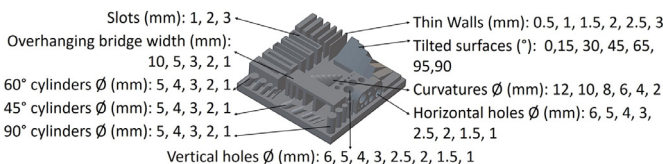


Fig. 3. The benchmark CAD drawing with the associated feature sizes.

Flat 2 mm thick dogbone tensile specimens were sliced using wire electro-discharge machining from horizontally made parts (Fig. 4). At least four specimens in each as-printed set were tested with extensometer and a strain rate of  $0.0067 \text{ s}^{-1}$  at room temperature in an Instron 4505 tensile testing machine.

### 3. Results and discussion

#### 3.1. Process optimization and reliability

Fig. 5 shows the densities of EBM parts made by different linear energies. Accordingly, an optimal energy input of  $1.2 \text{ J mm}^{-1}$  can deliver dense parts. After this point, excessive energy input should be avoided to prevent part

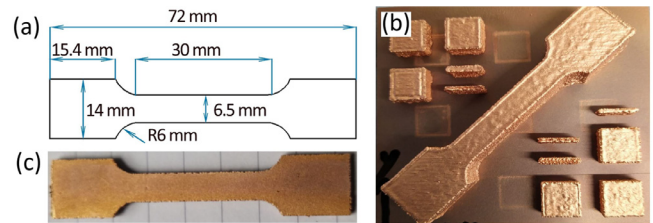


Fig. 4. Tensile bars from (a) design to (b) EBM printing and (c) specimen.

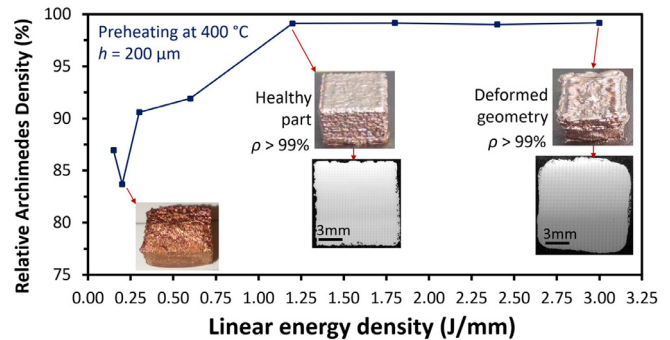


Fig. 5. Part density vs. energy input. Note: densities from Archimedes' principle could be lower than those calculable from cross-sections.

deformation due to high lateral heat conduction. After many optimizations on the correlative effects of beam power and scanning speed, the optimum values were  $P = 600 \text{ W}$  and  $s = 500 \text{ mm s}^{-1}$ .

Several sources of unreliability were identified for EBM processing of Cu here. These included powder reuse, loss of beam quality due to material spattering, unstable preheating, influence of the baseplate, smoking, and beam spot shape. Powder recycling was found to have only a weak effect. This could be actually beneficial, as it increased the flow (Fig. 1). Spattering was a significant factor, causing contamination of the top electron beam column. This could lead to some loss of beam control, necessitating regular maintenance. Implementing a stable preheating regime was also another issue, since it depended on the part geometry and build size. In fact, after starting the process from 400 °C, the melting of a bulky Cu component may even exceed the preheating temperature without a need for an extra preheating stage. Therefore, this must be considered on a case-by-case basis. The baseplate also had a significant effect. As pure Cu rapidly dissipates heat, it made it difficult to maintain temperature in the powder bed. Cu is also soft and hence easily deformed at a high temperature. These were not acceptable, so stainless steel was selected. Smoking was another issue. This occurred for thin and tall parts, as their melting did not provide sufficient energy to keep the powder bed temperature. In such cases, a more intense or longer preheating stage is necessary to maintain the temperature at 400 °C throughout the build.

The focal spot size appeared to be a critical factor, despite not appearing in the expression for energy density,  $E$ . The focal spot size is controlled using a parameter called focus offset (FO), which is an electronic current used for regulating the electromagnetic focusing lenses. According to our previous work, the EB was fully focused at  $FO = 10 \text{ mA}$  [12]. Using this fully focused position, a deep but narrow melt pool can form. This helps to reduce the spattering and to regulate the solidification by allowing an uninterrupted and consistent shrinkage (Fig. 6b and e). In contrast, when the focal point is above the powder bed surface (negative defocusing, see Fig. 6a,d and h), the EB diverges on the melt. This can create a shallower melt pool in the form of an inverted funnel. Therefore, the successive transport of melt from the surface to counteract solidification and shrinkage could easily be choked off when the beam moves away. This creates large voids on the surface. Conversely, when the focal point is below the surface (positive defocusing, see Fig. 6c,f and h), the beam is not yet converged when it meets the powder bed and could become narrower as the electrons penetrate into the material. Although this does not fail the process, the spattering can be enhanced due to the less concentrated heat provided by the larger spot size. Accordingly, the spot shape can be a source for unreliability of Cu EBM since this parameter may vary between machines or even builds.

Surprisingly, hatch spacing had only a small influence on the density in the range tested. This was since every hatch spacing tried led to an integrated surface without any visible defects and, hence, dense parts (Fig. 7). Nevertheless, a hatch spacing of 100 µm resulted in a visually smoother surface (Fig. 7a). This may increase the layer-by-layer process reliability and density.



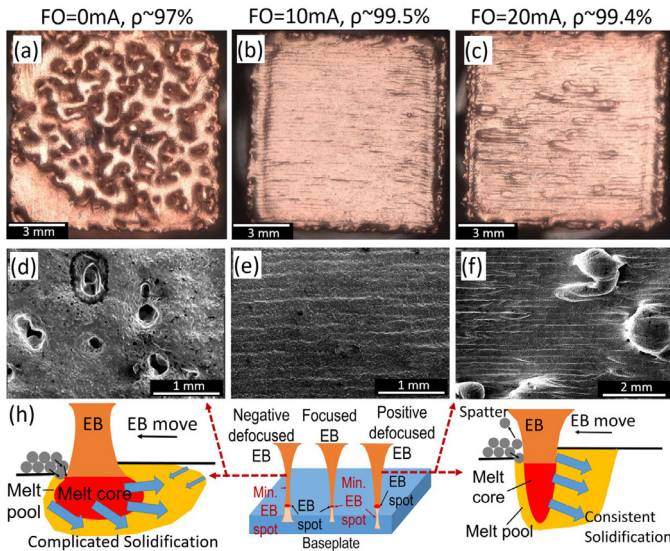


**Fig. 6.** Influence of beam spot on defect formation and EBM reliability. The negative defocused EB in the left schematic of (h) corresponds to the situation in (a) and (d), while positive defocused EB in the right schematic of (h) corresponds to (c) and (f). All parts are made with  $P = 600$  W,  $s = 500$  mm s<sup>-1</sup>, and  $h = 100$   $\mu$ m.

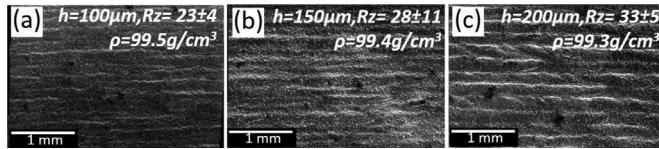


**Fig. 7.** Effect of hatch spacing on surface integrity (FO=10 mA).

### 3.2. Optimization of geometrical integrity, accuracy and roughness

Fig. 8b demonstrates that higher hatch spacing of 200  $\mu$ m can successfully create overhangs and horizontal cylinders without any support due to its lower corresponding energy. This is another advantage compared to SLM of Cu, where support for overhangs is critical. In contrast to a hatch spacing of 200  $\mu$ m, 100  $\mu$ m is preferable to create smooth surfaces and ensuring reliability by reaching a higher density for bulky parts (Fig. 8a). This is associated with reduced spattering due to the higher input energy. However, such a hatching strategy may fail to manufacture overhangs and hollow features.

To further increase the geometrical precision, three continuous contours with different energy levels were tested at FO=10 mA. Since these were (i) low, (ii) medium, (iii) high energy continuous contours, they were coded as LECC, MECC, HECC, respectively. A complete experimental analysis on different contour overlaps and sequences was performed and the most successful trials are summarized in Table 1. Two main criteria to select appropriate contours were surface roughness and the pore fraction down to 2 mm underneath the surface (i.e., border pore fraction). Here, MECC led to the smoothest side surface roughness and minimal surface notches and pores (Fig. 9). These improvements are attributed to creating a tiny gap between the powder and contour before the actual hatching as well as eliminating the edge irregularities [13].

After selecting MECC as the best contouring strategy, Fig. 10 shows how hatch spacing in conjunction with the utilized contouring influence the geometrical mismatch. The smaller hatch spacing has typically less mismatch (greener) for bulky features in Fig. 10a. However, the part with contouring is more deformed when  $h = 100$   $\mu$ m. It seems the heat has been maintained at the hatching cross section when a start contouring is used. This has led to a larger

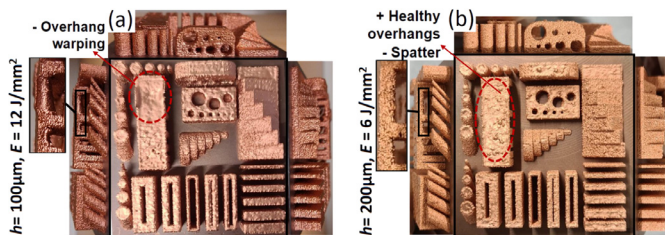


**Fig. 8.** The benchmarks made with different hatch spacing (FO=10 mA).

**Table 1.**

Selected scenarios for various contouring strategies.

Start contour	Energy (J/mm)	Track width ( $\mu$ m)	Overlap (%)	Border pore fraction (%) <sup>*</sup>	Side $R_z$ ( $\mu$ m)
Hatching	1.2	480 $\pm$ 70	N/A	2.25	123 $\pm$ 20
LECC	1.2	480 $\pm$ 70	75	0.80	84 $\pm$ 15
MECC	3	600 $\pm$ 40	75	0.37	83 $\pm$ 26
HECC	9	880 $\pm$ 60	50	0.56	89 $\pm$ 25

<sup>\*</sup> The porosity down to 2 mm underneath the surface (see also [13]).



**Fig. 9.** Effect of contour on the superficial defects along the edges (at left) of the cross section ( $h = 200$   $\mu$ m, FO=10 mA). BD: Building direction.

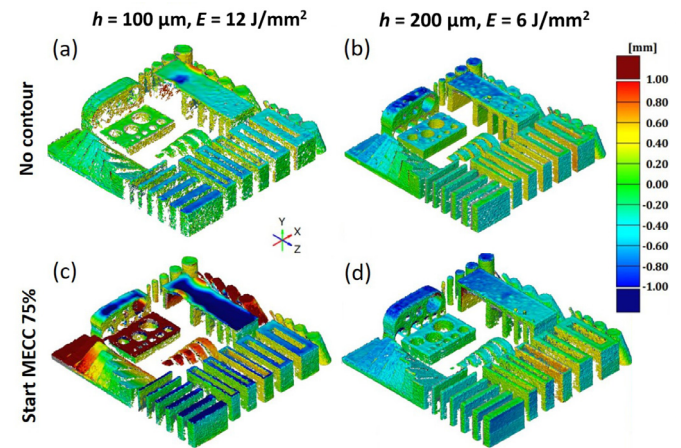


**Fig. 10.** Geometrical mismatch of benchmark parts made with different contouring and hatch spacing.

mismatch, since the energy density was already very high. Moreover, this figure shows that contour can be successfully applied in combination with the higher hatching inputting a lower energy. In fact, this can improve the geometrical possibilities to manufacture complicated features (see 'MECC +  $h = 200$   $\mu$ m' in Table 2). For small inner holes, no MECC might be still preferable as lateral heat can expand the actual feature.

**Table 2.**

Cu EBM printability of different features in Fig. 10.

Feature (all feature sizes are in mm)	$h = 100$ $\mu$ m	MECC + $h = 100$ $\mu$ m	$h = 200$ $\mu$ m	MECC + $h = 200$ $\mu$ m
Min Rod Diameter: made 90°, 60°, 45°	1.6, 1.4, 1.3	1.1, 0.9, 1.0	1.3, 1.3, 1.2	<b>1.0, 0.9, 1.0</b>
Min wall thickness	1.4	1.1	<b>1.0</b>	<b>1.0</b>
Min Horiz. hole Dia	1.1	1.0	<b>1.2</b>	<b>1.2</b>
Min Vert. hole Dia	1.0	1.3	<b>0.9</b>	1.1
Max Overhanging	4.2	4.9	9.4	<b>9.6</b>

### 3.3. Microstructure and mechanical reliability

The microstructure of EBM made Cu is shown in Fig. 11. As seen, the microstructure is very homogeneous, showing merely rather fine and polygonal grain cells below 40  $\mu$ m in size. Although this is rather uncommon in EBM (normally long columnar grains form/grow at high temperature [14]), this could be due to the rather low preheating temperature to process Cu here. Moreover, it seems that material impurities (e.g., Cu<sub>2</sub>O particles [15]) have acted as numerous nucleation sites enabling such a homogenous microstructure in both the powder layer plane and building plane.

Nevertheless, this highly homogenous microstructure is very interesting, as it could represent a strong texture. In this work, the room temperature Young's modulus,  $E$ , of the printed parts in horizontal direction is 80–86 GPa, which is lower than polycrystalline annealed Cu (110–130 GPa). This might be due to

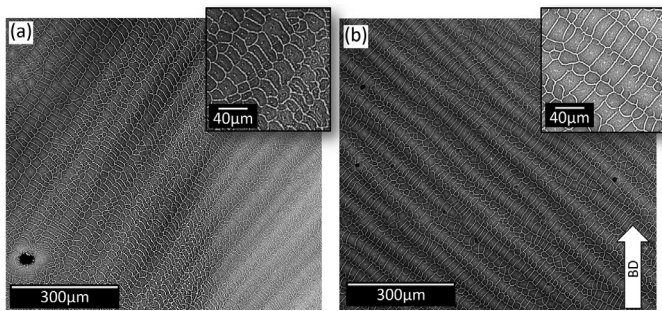


Fig. 11. EBM microstructure of Cu: (a) X-Y and (b) building sections.

the mechanical anisotropy indicative of texture, since  $E = 191.4$  GPa in (111) directions and  $E = 67.0$  GPa in (100) directions at 300 K [16]. Porosity from different builds exerts a level of unreliability in the tensile properties, but this influence was rather limited at the current densities which were over 99% (Fig. 12). This success was partly due to the application of 100 µm hatching which could deliver smooth additive surfaces, enabling dense parts in larger sizes.

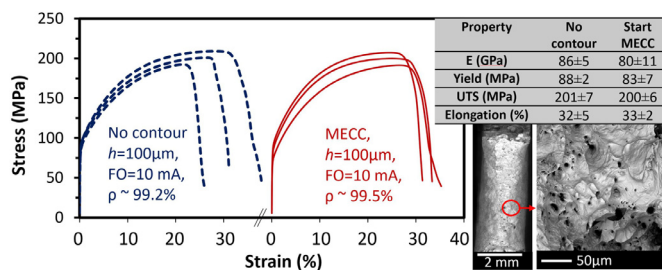


Fig. 12. Tensile properties of EBM printed Cu, made with  $h = 100$  µm.

#### 4. Summary

This work looked into identifying the processing challenges affecting the reliability as well as increasing the geometrical precision/possibilities of EBM Cu parts. After manufacturing dense material, it was found that unreliability is largely linked to parameters that are not typically considered within the expression for energy density. For example, powder preheating temperature is an important parameter which was suggested to be around 400 °C here. This was to reach minimal powder caking, high geometrical stability and high density. However, since the powder temperature profiles vary for EBM of Cu on a case-by-case basis, the associated parameters such as preheating duration should be set accordingly. The other important parameter for unreliability was the beam spot shape, which can vary from one machine or even one build to another. More specifically, having a focal point above the powder surface increased the surface voids, while a focal point below the powder surface enhanced the material spattering.

Hatch spacing influenced the surface roughness and geometrical precision, despite not exerting much influence on the density of small 10 mm cubic samples. However, the lower hatch spacing used (100 µm) smoothed the top surfaces, which could contribute to the manufacturing of reliable and dense parts with larger sizes. This lower hatch spacing though reduced the geometrical freedom (including overhangs) due to the larger associated melt pools. Therefore, lower hatch spacing can be applied for bulky cross sections while higher hatch spacing is recommended for

more complex geometries with internal features. Another parameter for geometrical precision was found to be contouring. Continuous contouring with a track width slightly larger than the hatching is suggested before hatching in this work. This can reduce the border pore fraction, smoothen the side roughness, and increase the geometrical precision and freedom.

#### Declaration of Competing Interest

The authors declare that they have no known competing financial interests or personal relationships that could have appeared to influence the work reported in this paper.

#### Acknowledgment

The authors gratefully acknowledge support from the Research Initiative on Sustainable Industry and Society (IRIS) and the Excellence in Production Research (XPRES) at KTH.

#### References

- [1] Bourell D, Kruth JP, Leu M, Levy G, Rosen D, Beese AM, Clare A (2017) Materials for Additive Manufacturing. *CIRP Annals* 66:659–681.
- [2] Dadbakhsh S, Speirs M, Kruth JP, Van Humbeeck J (2015) Influence of SLM on Shape Memory and Compression Behaviour of NiTi Scaffolds. *CIRP Annals* 64:209–212.
- [3] Schmidt M, Merklein M, Bourell D, Dimitrov D, Hausotte T, Wegener K, et al. (2017) Laser Based Additive Manufacturing in Industry and Academia. *CIRP Annals* 66:561–583.
- [4] Jadhav SD, Dadbakhsh S, Goossens L, Kruth JP, Van Humbeeck J, Vanmeensel K (2019) Influence of Selective Laser Melting Process Parameters on Texture Evolution in Pure Copper. *Journal of Materials Processing Technology* 270:47–58.
- [5] Vaneker T, Bernard A, Moroni G, Gibson I, Zhang Y (2020) Design for Additive Manufacturing: Framework and Methodology. *CIRP Annals* 69:578–599.
- [6] Galati M, Iuliano L (2018) A Literature Review of Powder-Based Electron Beam Melting Focusing on Numerical Simulations. *Addit Manuf* 19:1–20.
- [7] Milberg J, Sigl M (2008) Electron Beam Sintering of Metal Powder. *Production Engineering* 2:117–122.
- [8] Zhao X, Rashid A, Strondl A, Hulme-Smith C, Stenberg N, Dadbakhsh S (2021) Role of Superficial Defects and Machining Depth in Tensile Properties of Electron Beam Melting (EBM) Made Inconel 718. *Journal of Materials Engineering and Performance* 30:2091–2101.
- [9] Frigola P, Harrysson OA, Horn TJ, West HA, Aman RL, Rigsbee JM, et al. (2014) Fabricating Copper Components with Electron Beam Melting. *Advanced Materials and Processes* 172:20–24.
- [10] Lodes MA, Guschlbauer R, Körner C (2015) Process Development for the Manufacturing of 99.94% Pure Copper Via Selective Electron Beam Melting. *Materials Letters* 143:298–301.
- [11] Raab SJ, Guschlbauer R, Lodes MA, Körner C (2016) Thermal and Electrical Conductivity of 99.9% Pure Copper Processed via Selective Electron Beam Melting. *Advanced Engineering Materials* 18:1661–1666.
- [12] Lin Z, Zhao X, Dadbakhsh S, Rashid A (2021) Evaluating the Electron Beam Spot Size in Electron Beam Melting Machines. In: *Proceedings of the Virtual Lamdamap 14th International Conference & Exhibition, 10th–11th March 2021*
- [13] Zhao X, Dadbakhsh S, Rashid A (2021) Contouring Strategies to Improve the Tensile Properties and Quality of EBM Printed Inconel 625 Parts. *Journal of Manufacturing Processes* 62:418–429.
- [14] Guschlbauer R, Burkhardt AK, Fu Z, Körner C (2020) Effect of the Oxygen Content of Pure Copper Powder on Selective Electron Beam Melting. *Materials Science and Engineering A* 779:139106.
- [15] Ramirez DA, Murr LE, Martinez E, Hernandez DH, Martinez JL, Machado BI, et al. (2011) Novel Precipitate–Microstructural Architecture Developed in the Fabrication of Solid Copper Components by Additive Manufacturing Using Electron Beam Melting. *Acta Materialia* 59:4088–4099.
- [16] Pal-Val P, Pal-Val L, Natsik V, Davydenko A, Rybalko A (2015) Giant Young's Modulus Variations in Ultrafine-Grained Copper Caused by Texture Changes at Post-Spd Heat Treatment. *Archives of Metallurgy and Materials* 60:3073–3076.